

RESEARCH ARTICLE

SOLAR CELLS

Stabilized hole-selective layer for high-performance inverted p-i-n perovskite solar cells

Zhen Li^{1†}, Xianglang Sun^{1, 2†}, Xiaopeng Zheng^{3, 4†}, Bo Li^{1†}, Danpeng Gao¹, Shoufeng Zhang¹, Xin Wu¹, Shuai Li¹, Jianqiu Gong¹, Joseph M. Luther³, Zhong'an Li^{2*}, Zonglong Zhu^{1*}

P-i-n geometry perovskite solar cells (PSCs) offer simplified fabrication, greater amenability to charge extraction layers, and low-temperature processing over n-i-p counterparts. Self-assembled monolayers (SAMs) can enhance the performance of p-i-n PSCs but ultrathin SAMs can be thermally unstable. We report a thermally robust hole-selective layer comprised of nickel oxide (NiO_x) nanoparticle film with a surface-anchored (4-(3,11-dimethoxy-7H-dibenzo[c,g]carbazol-7-yl)butyl)phosphonic acid (MeO-4PADBC) SAM that can improve and stabilize the NiO_x/perovskite interface. The energetic alignment and favorable contact and binding between NiO_x/MeO-4PADBC and perovskite reduced the voltage deficit of PSCs with various perovskite compositions and led to strong interface toughening effects under thermal stress. The resulting 1.53-electron-volt devices achieved 25.6% certified power conversion efficiency and maintained >90% of their initial efficiency after continuously operating at 65 degrees Celsius for 1200 hours under 1-sun illumination.

Phosphonic acid self-assembled monolayers (SAMs) with a carbazole core have enabled performance advances in perovskite solar cells (PSCs), for both single-junction (1–4) and perovskite-based tandem solar cells (5–9), because of their high hole selectivity, fast hole transfer rate, and low interfacial trap state density (10–13). However, compared with conventional polymeric and metal oxide hole transporting materials, SAM-based PSCs have exhibited poorer thermal stability (14–18). The investigation of the device's operational stability, with electrical bias under maximum power point (MPP) operation or at open-circuit voltage (V_{OC}), under elevated temperatures (65° to 85°C) is critical to improve the confidence in their stability and to meet the qualification of international stability standards (i.e., International Summit on Organic Photovoltaic Stability (ISOS) and International Electrochemical Commission 61215 standards) (19). Whereas most studies on the SAM-based PSCs have reported the operational stability at room temperature or enhanced the device's durability under thermal stress by stabilizing perovskite surface and bulk (20, 21), the degradation effect of SAM-forming molecules under elevated tem-

perature (>65°C) have rarely been discussed (fig. S1 and table S1). The thermal stability of SAM-forming molecules depends largely on their bonding to the selected substrates, as the bond between the anchoring group and the spacer of the molecule can be broken through temperature-induced desorption (22–25).

We report a new SAM, (4-(3,11-dimethoxy-7H-dibenzo[c,g]carbazol-7-yl)butyl)phosphonic acid (MeO-4PADBC), which we anchored to the NiO_x film to fabricate inverted p-i-n PSCs (fig. S2). The NiO_x/MeO-4PADBC exhibited an optimal dipole moment and amenable surface for favorable contact with perovskite that resulted in an ideal energetic alignment, fast hole extraction, and low defect density. Such an interface configuration also immobilized the SAM molecules at the NiO_x/perovskite interface and produced a robust hole-selective layer (HSL) for thermally stable PSCs that had thermal-degradation activation energy ~3 times greater than that for ITO/MeO-4PADBC. These synergetic effects enabled 1.53-electron volt (eV) p-i-n PSCs V_{OC} of 1.19 V (95% of calculated potential) and a verified power conversion efficiency (PCE) of 25.6%. 1.68- and 1.80-eV-wide bandgap perovskite composition devices also showed encouraging PCEs of 22.7 and 20.1%, respectively. Moreover, 1.53-eV PSCs using NiO_x/MeO-4PADBC HSL maintained >90% of initial efficiency in long-term operational stability tests under 65°C for 1200 hours, and extrapolation of the Arrhenius energy indicates that the solar cells should maintain 80% of initial efficiency for more than 10 months at 25°C.

SAM design and synthesis

Modulating the terminal functional group is an effective way to tune the interfacial interactions between SAMs and perovskite. For ex-

ample, the introduction of two methoxy groups (OMe) into [2-(9H-carbazol-9-yl)ethyl]phosphonic acid (2PACz) enabled a new SAM, [2-(3,6-dimethoxy-9H-carbazol-9-yl)ethyl]phosphonic acid (MeO-2PACz), which improved the interfacial contact and enabled a higher efficiency of p-i-n PSC compared with 2PACz (10). Nonetheless, the OMe substitution on the carbazole core also caused a decrease in dipole moment from ~2.0 D of 2PACz to ~0.2 D of MeO-2PACz, which in turn led to the offset between the highest occupied molecular orbital (HOMO) of the SAM molecule and the valence band maximum (VBM) of the perovskite (10, 26). This phenomenon can be ascribed to high planarity and symmetry of the carbazole structure; the incorporation of two OMe groups with opposite directions of dipole moment resulted in a net molecular dipole moment of MeO-2PACz close to zero (Fig. 1A). We addressed this issue by using a non-coplanar screw-shaped dibenzo[c,g]carbazole (DBC) unit as the core to reduce the negative effect on the dipole moment when introducing OMe groups, affording a new SAM of MeO-4PADBC (Fig. 1B). Density functional theory (DFT) calculations verified that MeO-4PADBC only has a slightly decreased dipole moment (2.4 D) compared with that of (4-(7H-dibenzo[c,g]carbazol-7-yl)butyl)phosphonic acid (4PADBC) (2.9 D), which is quite different from those obtained for carbazole-based SAMs (figs. S3 and S4).

The synthetic route of MeO-4PADBC is shown in fig. S5, along with structural characterizations presented in figs. S6 to S9. The calculated HOMO and lowest unoccupied molecular orbital distributions are shown in fig. S10, with values of –4.91 and –1.15 eV, respectively. To gain a deeper insight of the SAM molecule structure, we grew a single crystal of 3,11-dimethoxy-7H-dibenzo[c,g]carbazole (MeO-DBC, CCDC number: 2279245), which lacks the anchoring group that would disrupt intermolecular interactions. As shown in fig. S11, A and B, two naphthalene rings are located on different sides of the pyrrole ring and exhibit a dihedral angle of 12.44°, which greatly reduces the planarity and symmetry of the skeleton structure to enable a negligible effect on the dipole moment when introducing OMe groups. Moreover, the MeO-DBC core had a slipped π -stacked packing motif with strong C-H... π (2.72 Å) and π - π (3.79 Å) interactions (fig. S11C), which could induce a highly ordered one-dimensional assembly that favors a dense, tilted, highly ordered monolayer on the substrate (fig. S11D) (9, 27, 28).

We then calculated the interfacial binding energies between SAMs and perovskite, showing that MeO-4PADBC has a stronger binding with perovskite with a total binding energy (E_b) of –7.19 eV, compared with that of –5.27 eV for MeO-2PACz (fig. S12). The main electrostatic interaction of the calculated SAMs is the O atoms from OMe groups with the Pb from

¹Department of Chemistry, City University of Hong Kong, Kowloon 999077, Hong Kong. ²State Key Laboratory of Materials Processing and Die & Mould Technology, Key Laboratory for Material Chemistry of Energy Conversion and Storage, Ministry of Education, School of Chemistry and Chemical Engineering, Huazhong University of Science and Technology, Wuhan, 430074, P.R. China. ³National Renewable Energy Laboratory, Golden, CO 80401, USA.

⁴Center of Materials Science and Optoelectronics Engineering, College of Materials Science and Optoelectronic Technology, University of Chinese Academy of Science, Beijing, 100049, P.R. China.

*Corresponding author. Email: zonglizu@cityu.edu.hk (Z.Z.); lizha@hust.edu.cn (Zho.L)

†These authors contributed equally to this work.

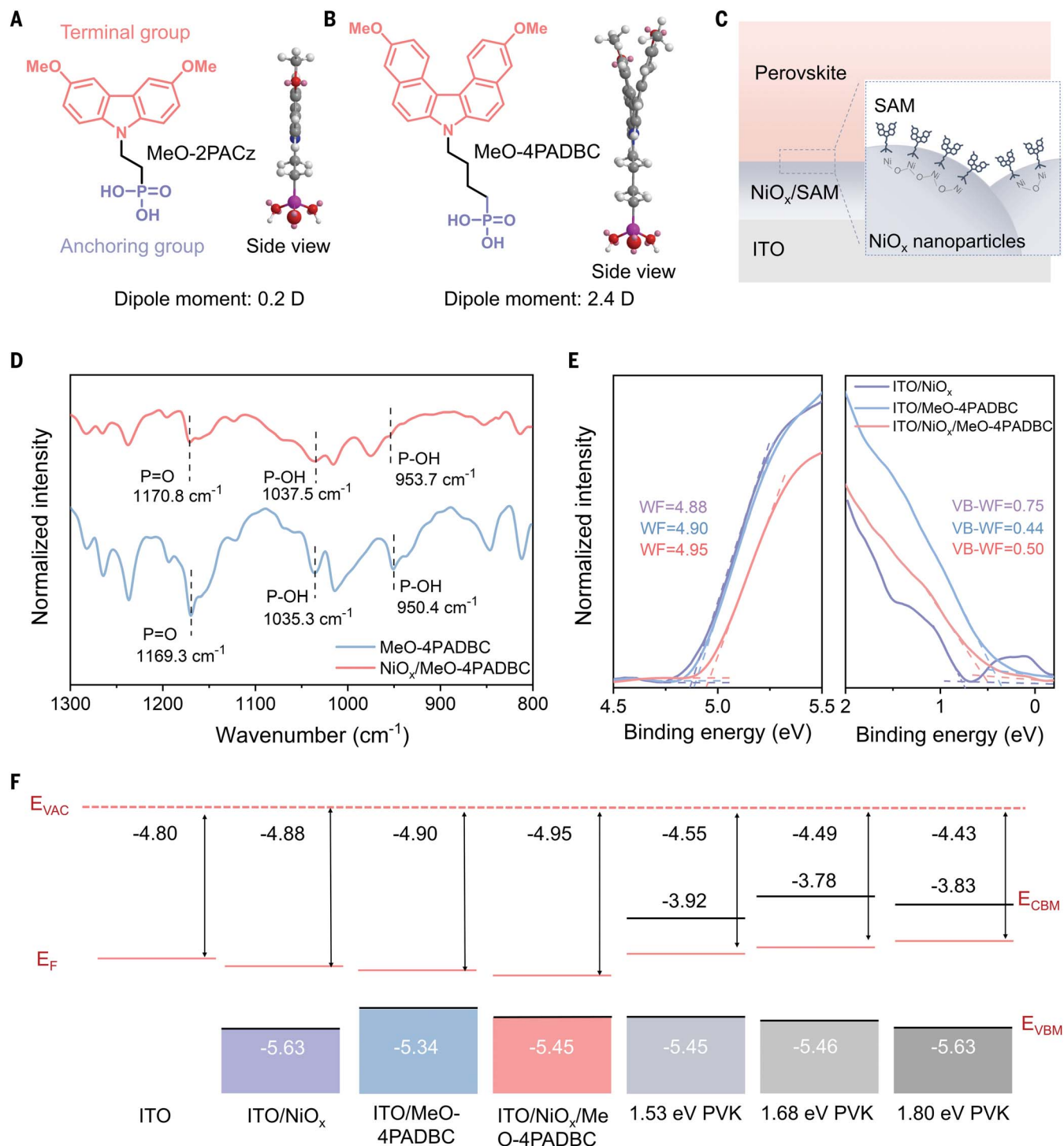


Fig. 1. Molecular structure and electrical properties of HSLs. Molecular structure and side view of (A) MeO-2PACz and (B) MeO-4PADBC. (C) Schematic illustration of MeO-4PADBC anchoring on NiO_x nanoparticle as the HSL in PSC. (D) FTIR spectra of MeO-4PADBC and NiO_x/MeO-4PADBC. (E) UPS spectra of ITO substrates covered by NiO_x, MeO-4PADBC, and NiO_x/MeO-4PADBC. (Left) UPS spectra around the secondary electron cutoff (WF, work function);

(right) UPS spectra in the valence band (VB) region. (F) Schematic representation of the band edge positions of the studied HSLs based on values from UPS measurements, referenced to the vacuum level. E_F and E_{VAC} represent Fermi and vacuum levels, respectively. E_{VB} and E_{CBM} represent the energy of valence band maximum and conduction band minimum, respectively.

perovskite, however MeO-4PADBC has a more energetically favorable contact with perovskite compared with MeO-2PACz, which can be ascribed to the more concentrated electron

distribution of the coordinated OMe group on MeO-4PADBC than that on MeO-2PACz (fig. S13). Moreover, Bader charge analysis also suggests a stronger Pb-O interaction

between MeO-4PADBC and perovskite with a shorter calculated interaction length of 4.7 Å than that of MeO-2PACz of 4.9 Å (fig. S14), which can be further confirmed by the results

of ^1H NMR spectra of the SAMs in DMSO- d_6 with or without mixing with PbI_2 (fig. S15).

Hole-selective layer applications

We compared MeO-4PADBC SAM and $\text{NiO}_x/\text{MeO-4PADBC}$ as the HSLs for p-i-n PSCs (Fig. 1C). Fourier-transform infrared (FTIR) spectra were then collected by scraping the MeO-4PADBC and $\text{NiO}_x/\text{MeO-4PADBC}$ films off the substrates to amplify the signal, in which the P=O (1169 cm^{-1}) and P-OH (1035 and 950 cm^{-1}) absorption peaks show a clear shift (Fig. 1D), indicating the formation of a chemical bond (29). This can be further confirmed by the changes of the $\text{Ni } 2p$ core level of NiO_x and $\text{NiO}_x/\text{MeO-4PADBC}$ films deposited on the indium tin oxide (ITO) substrates obtained by x-ray photoelectron spectroscopy (XPS) spectra (fig. S16). The crystal structure and absorbance of representative perovskite film with a composition of $\text{Cs}_{0.05}\text{FA}_{0.85}\text{MA}_{0.1}\text{PbI}_3$ on both substrates remained unchanged (figs. S17 and S18). However, the perovskite deposited on ITO/ $\text{NiO}_x/\text{MeO-4PADBC}$ substrate had larger crystal domains than those on control substrates (fig. S19). This is because of the denser anchoring of SAM molecules onto the ITO/ NiO_x substrate through more robust tridentate binding absorption, which can not only reduce the surface roughness of ITO/ NiO_x substrate (30–32) (figs. S20 and S21), but also lead to a more hydrophobic surface (fig. S22) and stronger interaction between perovskite and SAM molecules (33–35). These synergetic effects contribute to facilitating the perovskite crystal nucleation and growth, thus enhancing the perovskite crystallization.

We further used ultraviolet photoelectron spectroscopy (UPS) to assess the energetic alignment of different substrates relative to perovskite absorbers with different bandgaps (1.53, 1.68, and 1.8 eV, see Fig. 1E and fig. S23), and the results are summarized in Fig. 1F. The HOMO energy levels are -5.34 eV for ITO/MeO-4PADBC and -5.45 eV ITO/ $\text{NiO}_x/\text{MeO-4PADBC}$, respectively, and the work function (Φ) of the latter substrate is deeper than that of the former one (-4.95 versus -4.90 eV), indicative of better energetic alignment with different perovskite absorbers. However, upon application of the carbazole-based SAM molecules onto the ITO/ NiO_x surface, the ITO/ $\text{NiO}_x/\text{MeO-2PACz}$ system exhibited an upward shift of the Φ , in contrast to the ITO/ $\text{NiO}_x/2\text{PACz}$ substrate (26, 36) (fig. S24). This phenomenon can be attributed to the incorporation of OMe groups on 2PACz, which considerably reduced the dipole moment. This reduction can be explained by the highly planar carbazole motif, as discussed earlier. Time-resolved photoluminescence (TRPL) decay data showed a decreased carrier lifetime from 925.5 ns for the perovskite on ITO to 42.9 and 32.3 ns for the perovskite on ITO/MeO-4PADBC and ITO/ $\text{NiO}_x/\text{MeO-4PADBC}$, respectively, indicating a more facilitated hole extraction resulted

by the ITO/ $\text{NiO}_x/\text{MeO-4PADBC}$ substrate (fig. S25 and table S2).

Solar cell performance and characterization

We further evaluated the photovoltaic performance of PSCs with a p-i-n device configuration: glass/ITO/HSL/perovskite/two-dimensional (2D) passivation layer/ C_{60} /bathocuproine (BCP)/Ag (Fig. 2A). The 2D passivation layer was a mixture of 4-trifluorophenylethylammonium iodide ($\text{CF}_3\text{-PEAI}$) and methylammonium iodide (MAI) with an optimal volume ratio of 3:1 (4). The cross-section scanning electron microscopy (SEM) images of the PSC (1.53 eV) showed a thickness of ~ 715 nm for the perovskite films (fig. S26). The device with $\text{NiO}_x/\text{MeO-4PADBC}$ as the HSL (1.53 eV) showed negligible hysteresis and had a high verified PCE of 25.6% for a mask area of 0.0414 cm^2 (figs. S27 and S28), with a V_{OC} of 1.19 V, a short-circuit current density (J_{SC}) of 25.4 mA cm^{-2} , and a fill factor (FF) of 84.6%, which outperformed the MeO-4PADBC-based device (PCE = 24.2% with $V_{\text{OC}} = 1.16$ V, $J_{\text{SC}} = 25.4\text{ mA cm}^{-2}$, and FF = 82.1%). The NiO_x control device without a SAM only showed a PCE of 21.6%, attributed to a mismatch of energetic alignment and high surface defect density on NiO_x film (37, 38) (Fig. 2B). Moreover, we have also conducted HSL engineering by applying carbazole-based SAM anchoring on NiO_x . The V_{OC} of the $\text{NiO}_x/\text{MeO-2PACz}$ -based device (1.15 V) is lower than that of the device with $\text{NiO}_x/2\text{PACz}$ (1.17 V) (figs. S29, A and B). This issue was addressed by replacing the carbazole motif with a nonplanar DBC core in SAM molecules (fig. S29, C and D). To better understand the mechanism of the improved V_{OC} and FF with the use of $\text{NiO}_x/\text{MeO-4PADBC}$ as HSL, we further conducted the FF loss (supplementary text and fig. S30) and V_{OC} loss calculations (supplementary text, fig. S31, and table S3). We observed that the improved V_{OC} and FF of $\text{NiO}_x/\text{MeO-4PADBC}$ were mainly attributed to the suppressed nonradiative recombination loss, indicating reduced trap state density at the HSL/perovskite interface.

Our $\text{NiO}_x/\text{MeO-4PADBC}$ strategy also worked effectively for 1.68- and 1.80-eV PSCs, resulting in PCEs of 22.7 and 20.1%, respectively (Fig. 2C, fig. S32, and table S4). Steady-state power output (SPO) confirmed the reliability of three bandgap devices, with stabilized PCEs of 25.5, 22.3, and 19.5% for 1.53-, 1.68- and 1.80-eV, respectively (Fig. 2D). Additionally, the calculated J_{SC} values from external quantum efficiency (EQE) of the champion devices were consistent with those extracted from the current density-voltage (J - V) measurements (fig. S33), and the derivatives of EQE spectra can further confirm the perovskite bandgaps applied here (fig. S34). We further presented the EQE with internal quantum efficiency (IQE) results of representative 1.53-eV device with HSLs of NiO_x , MeO-4PADBC, and $\text{NiO}_x/\text{MeO-4PADBC}$ in fig. S35. The IQE between 550 nm

to 700 nm is spectrally flat and approaches nearly 100% for both of MeO-4PADBC and $\text{NiO}_x/\text{MeO-4PADBC}$ -based devices, indicating efficient charge collection and transfer at the perovskite interface achieved by the incorporation of SAM (12, 39).

The defect density profiles were then studied to identify enhanced photovoltaic performance through the space charge limit current (SCLC) method (fig. S36). The hole-only devices with $\text{NiO}_x/\text{MeO-4PADBC}$ showed the lowest defect density of $1.96 \times 10^{15}\text{ cm}^{-3}$, compared with those with MeO-4PADBC ($2.91 \times 10^{15}\text{ cm}^{-3}$) and NiO_x ($3.81 \times 10^{15}\text{ cm}^{-3}$). In addition, the decreased slope of the light intensity dependence V_{OC} plot for $\text{NiO}_x/\text{MeO-4PADBC}$ -based devices supported a reduced interfacial trap density at the HSL/perovskite interface (40) (fig. S37). We note that PSCs based on $\text{NiO}_x/\text{MeO-4PADBC}$ further demonstrated a lower leakage current than those on other HSLs (fig. S38), which we attributed to the compact NiO_x layer preventing the perovskite from contacting ITO through the pinholes in the ultrathin SAM layer. These results demonstrated that the $\text{NiO}_x/\text{MeO-4PADBC}$ HSL effectively increased the V_{OC} of the PSCs.

To quantify the interface losses, quasi-Fermi level splitting (QFLS) analysis for partial cell stacks was conducted. A laser wavelength of 375 nm was used to illuminate a PSC with 1-sun equivalent intensity by accommodating the generated current near J_{SC} under a standard solar simulator (41, 42) (supplementary text, fig. S39). As shown in Fig. 2E, the QFLS of ITO/ $\text{NiO}_x/\text{MeO-4PADBC}$ /perovskite stack was comparable to the glass/perovskite stack, with implied V_{OC} of 1.17 V versus 1.18 V for 1.53-eV perovskite film, 1.26 V versus 1.27 V for 1.68-eV perovskite film, and 1.35 V versus 1.36 V for 1.80-eV perovskite film, respectively. These results indicated a low voltage loss on the interface between $\text{NiO}_x/\text{MeO-4PADBC}$ and perovskites.

We further performed the QFLS measurements on the ITO/HSL/perovskite/passivation layer/electron-transporting layer (ETL) stacks (Fig. 2F), with the V_{OC} s of the PSCs listed as a comparison. The differences between the QFLS of PSCs on ITO/ $\text{NiO}_x/\text{MeO-4PADBC}$ and the V_{OC} extracted from related J - V measurements were comparable, demonstrating spatially flat Fermi levels throughout the device and low energy offset on the HSL for carrier extraction (27, 28). It is noteworthy that the V_{OC} of our 1.53-eV devices (1.19 V) reached 95% of their calculated potential and the V_{OC} of our 1.68-eV (1.25 V) and 1.80-eV (1.34 V) devices also approached 90% of the calculated potential (Fig. 2G).

PSC stability studies

Previous reports have demonstrated that SAMs desorb under thermal stress from the anchored

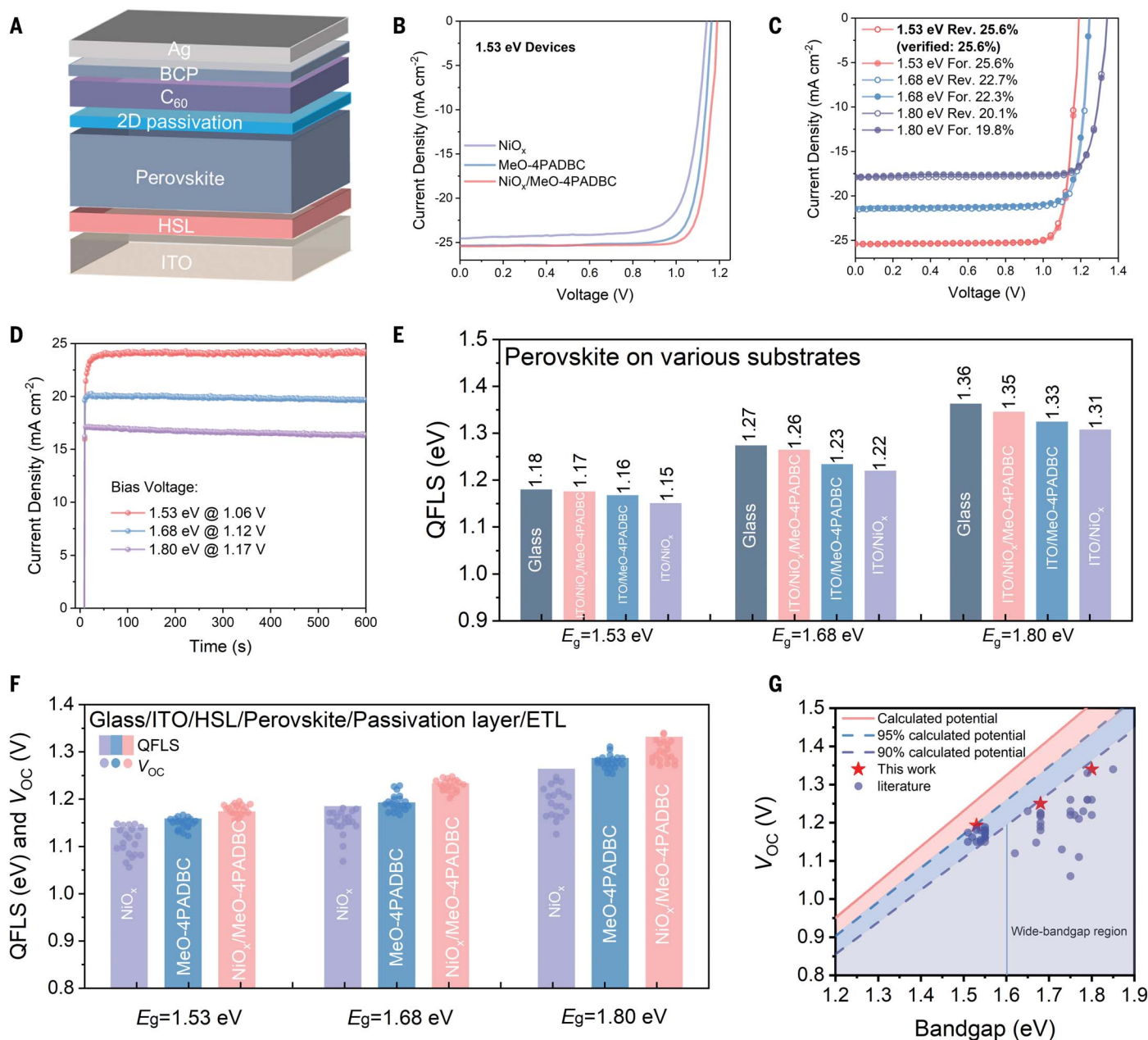


Fig. 2. Photovoltaic performance of PSCs with different HSLs. (A) Schematic illustration of p-i-n PSC. (B) J-V curves of the best-performing 1.53 eV devices with NiO_x, MeO-4PADBC, and NiO_x/MeO-4PADBC as HSL. (C) J-V curves of the best-performing NiO_x/MeO-4PADBC-based devices with bandgaps of 1.53, 1.68, and 1.80 eV (Rev., reverse scan; For., forward scan). (D) SPO at the MPP for the best-performing NiO_x/MeO-4PADBC-based PSCs with three bandgaps of perovskite

absorbers. (E) QFLS in the case of three bandgaps of perovskite with different HSLs. (F) Comparison of the V_{OC} of actual PSCs with the corresponding QFLS of representative layer stacks. (G) Comparison of the V_{OC} with different bandgaps of devices from the literature to our work. The line represents the V_{OC} extracted from calculated potential. The wide-bandgap region refers to 1.6 to 1.9 eV in the figure.

substrate (29, 30), but few effective solutions to this problem have been explored. To estimate the thermal stability of the ITO/NiO_x/MeO-4PADBC substrate, we applied Kelvin probe force microscopy (KPFM) to record the surface potential evolution of the SAM under heat treatment by taking pristine ITO/MeO-4PADBC as a reference. Before thermal aging, the ITO/MeO-4PADBC and ITO/NiO_x/MeO-4PADBC substrates both exhibited relatively uniform sur-

face potential with a narrow contact potential distribution (CPD) of ~40 mV, indicating that the SAM molecules were densely packed onto both of ITO and NiO_x surfaces (Fig. 3, A and B). After aging on a hotplate at 65°C for 1200 hours, the NiO_x/MeO-4PADBC substrate displayed negligible CPD changes, whereas the ITO/MeO-4PADBC CPD value increased to ~70 mV (Fig. 3, C and D). We propose that the fluctuations of CPD for the ITO/MeO-4PADBC substrate

could be attributed to desorption, morphological changes under thermal stress, or both.

To further explore the binding ability of SAM to the substrate under heating, DFT simulations were conducted to investigate the binding energies between MeO-4PADBC and ITO or NiO_x substrate at 300 K (~27°C) and 340 K (~67°C) (Fig. 3, E and F). MeO-4PADBC had a higher binding energy with NiO_x (~22.4 eV) than with ITO (~16.7 eV) at 300 K, suggesting

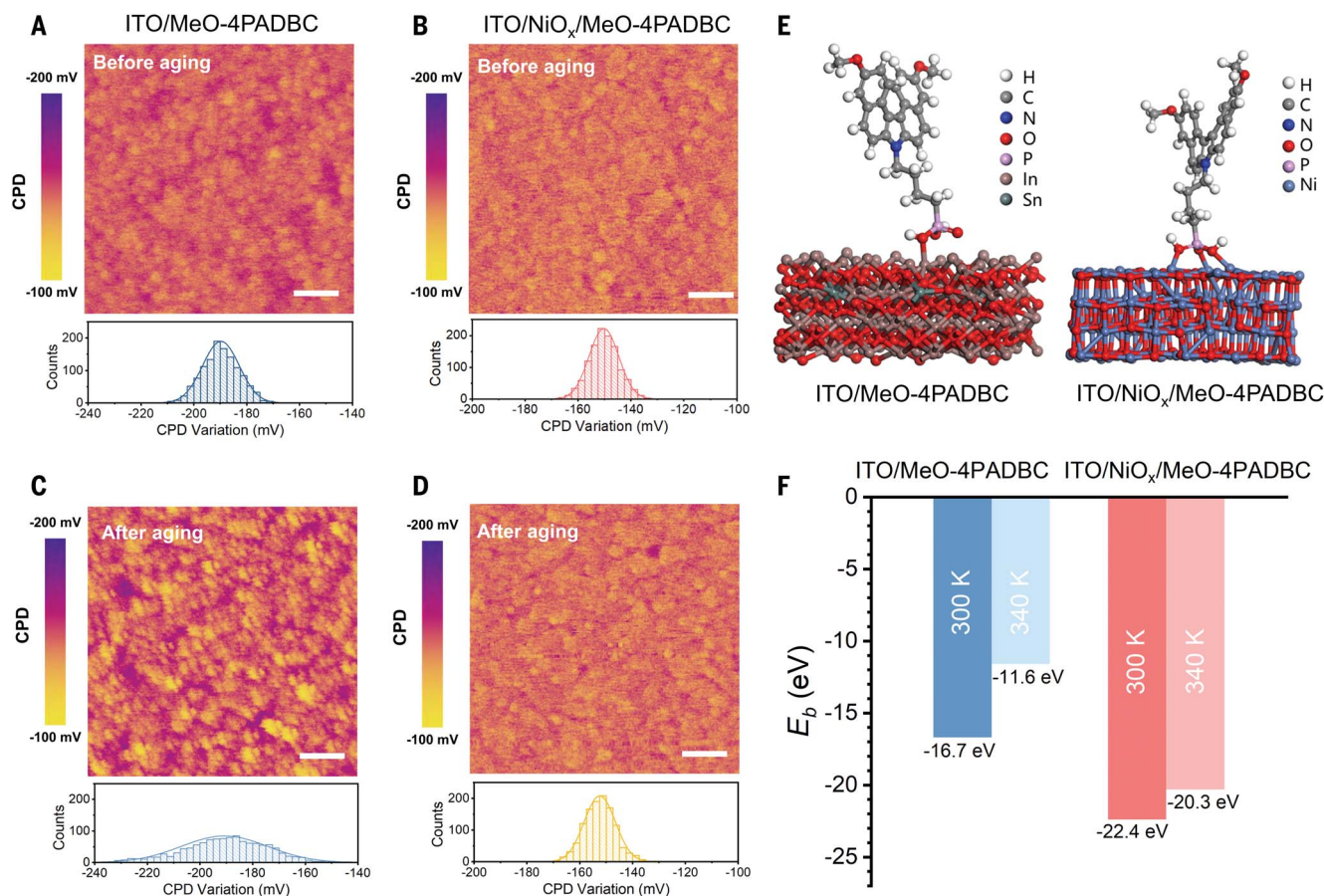


Fig. 3. Analysis of the degradation mechanism of PSCs. (A to D) Surface potential images obtained by scanning Kelvin probe microscopy (scale bar 500 nm) of the HSLs before and after aging at 65°C for 1200 hours. At the bottom of the figure are the statistical potential distributions of film surfaces. (E) DFT calculation of the binding energy of MeO-4PADBC with ITO and NiO_x. (F) Binding energies (E_b) of MeO-4PADBC with ITO and with NiO_x at the temperatures of 300 and 340 K.

a stronger bonding strength on the NiO_x film. This difference was attributed to the higher density of hydroxyl groups on the NiO_x surface than on the ITO, which is critical to the chemisorption of SAM on the metal oxide (43, 44). The tridentate binding between SAM and NiO_x was stronger than the bidentate binding between SAM and ITO (29, 45). At 340 K, the binding energy between SAM and ITO decreased from -16.7 to -11.6 eV, but that between MeO-4PADBC and NiO_x film showed minor changes (-20.3 eV). These results indicated that MeO-4PADBC on the NiO_x film is more robust against thermal stress compared with MeO-4PADBC on bare ITO.

Thermal accelerated aging measurements were conducted to evaluate the reliability of SAM-based PSCs. To avoid the influence of the 2D capping layer, the encapsulated devices without top passivation were prepared for stability testing. The initial J - V curves and photographs of the encapsulated devices are shown in fig. S40 and S41, respectively. The PSCs were operated under constant 1-sun illumination at fixed resistance loads near the MPP with the temperature ranging from

25° to 100°C, following the ISOS-L-2I procedure (19). The MeO-4PADBC-based devices degraded to 85 and 65% of starting PCEs after 1200 hours at 25°C and 65°C, respectively (Fig. 4A). When the aging temperature increased to 85°C, only 47% of its initial PCE was retained after 800 hours. The NiO_x devices retained 85 and 65% of initial PCEs at 65° and 85°C, respectively, after 1200 hours (Fig. 4B). However, the NiO_x/MeO-4PADBC-based devices retained 90 and 74% of initial PCEs after 1200 hours at 65° and 85°C, respectively (Fig. 4C), which was consistent with the degradation analysis in Fig. 3. Both devices based on NiO_x, MeO-4PADBC, or NiO_x/MeO-4PADBC as HSL showed a more obvious downward trend when the aging temperature was raised to 100°C. For a more comprehensive evaluation of the thermal stability of our NiO_x/MeO-4PADBC strategy, we further applied the PSCs with top passivation to conduct the operational stability at 65°C for 500 hours (fig. S42). The devices presented a slightly improved stability compared with the device without passivation at the same time stage, which maintained 96% of its initial PCE. This may be due to the

higher hydrophobic surface brought by the CF₃-PEAI passivation (46).

We then determined the activation energy (E_a) of the temperature-dependent degradation of our PSCs with different HSLs according to a previously reported method (supplementary text) (47). The E_a value of NiO_x/MeO-4PADBC-based devices (0.389 ± 0.022 eV) was almost three times higher than that of MeO-4PADBC-based devices (0.150 ± 0.017 eV). The lifetime acceleration factor (AF) of each temperature can be obtained from E_a (Fig. 4D), from which it can be estimated that PSCs with NiO_x/MeO-4PADBC HSL could retained 80% of its initial PCE at room temperature after 7567 hours operation, without top passivation treatment.

Conclusions

We have demonstrated an efficient and stabilized HSL with greatly improved thermal stability for high efficiency SAM-containing inverted p-i-n PSCs. Rational molecular structure design of MeO-4PADBC and in-depth analysis revealed that optimal dipole moment and favorable contact with perovskite are the

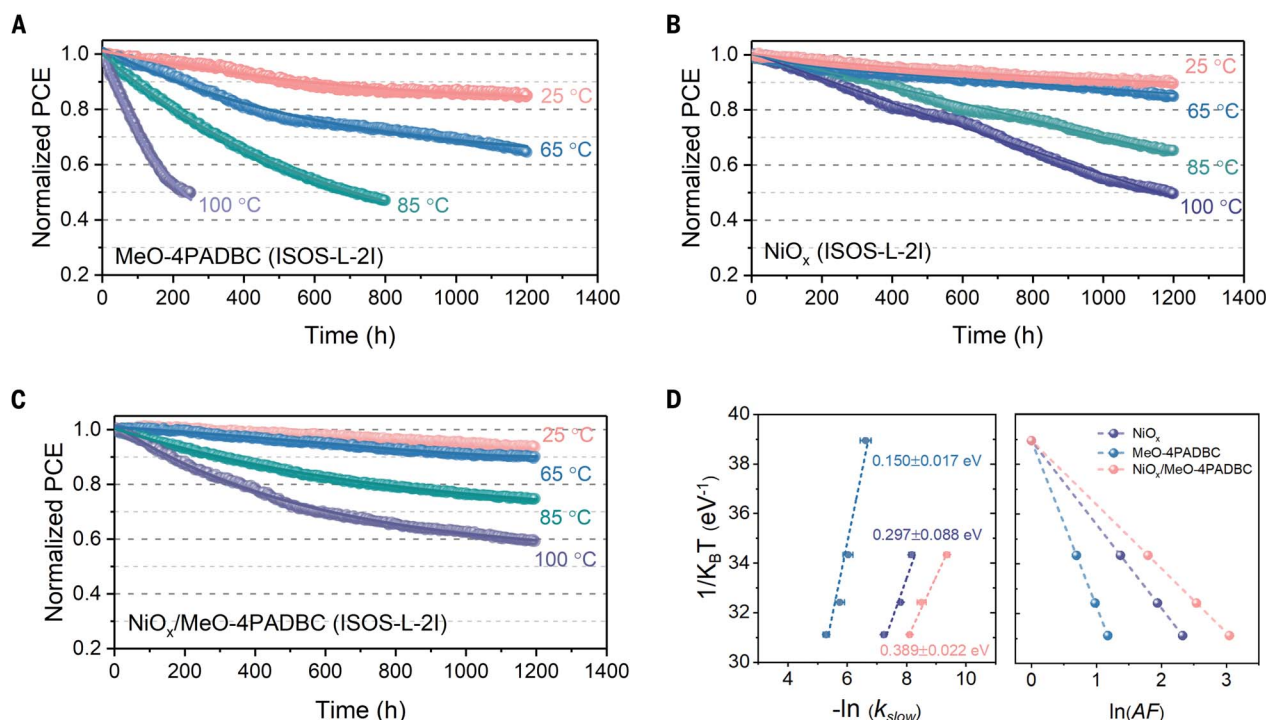


Fig. 4. Long-term stability assessment of PSCs under different temperatures. (A to C) Operational stability of PSCs with HSL of (A) MeO-4PADBC, (B) NiO_x , and (C) $\text{NiO}_x/\text{MeO-4PADBC}$ at temperatures of 25°, 65°, 85°, and 100°C, respectively. (D) Natural logarithm of slow degradation rate (k_{slow}) versus $1/k_B T$

keys to ideal energy alignment and fast hole extraction to improve the device efficiency and stability. Moreover, the anchoring of MeO-4PADBC SAM molecules on the NiO_x film can form a stronger tridentate bond with NiO_x , which effectively reduces the voltage loss and further maintains a strong fixation effect under thermal stress. Our study provides theoretical guidance for the design of efficient and stable HSL and paves the path for facile access to commercially available inverted p-i-n PSCs.

REFERENCES AND NOTES

- Q. Jiang et al., *Nature* **611**, 278–283 (2022).
- Q. Tan et al., *Nature* **620**, 545–551 (2023).
- S. Zhang et al., *Science* **380**, 404–409 (2023).
- X. Zheng et al., *Nat. Energy* **8**, 462–472 (2023).
- H. Chen et al., *Nature* **613**, 676–681 (2023).
- X. Y. Chin et al., *Science* **381**, 59–63 (2023).
- S. Mariotti et al., *Science* **381**, 63–69 (2023).
- K. O. Brinkmann et al., *Nature* **604**, 280–286 (2022).
- R. He et al., *Nature* **618**, 80–86 (2023).
- A. Al-Ashouri et al., *Energy Environ. Sci.* **12**, 3356–3369 (2019).
- A. Al-Ashouri et al., *Science* **370**, 1300–1309 (2020).
- I. Levine et al., *Joule* **5**, 2915–2933 (2021).
- F. H. Isikgor et al., *Nat. Rev. Mater.* **8**, 89–108 (2022).
- C. M. Crudden et al., *Nat. Chem.* **6**, 409–414 (2014).
- L. Srisombat, A. C. Jamison, T. R. Lee, *Colloids Surf. A Physicochem. Eng. Asp.* **390**, 1–19 (2011).
- H. Chen et al., *Nat. Photonics* **16**, 352–358 (2022).
- X. Li et al., *Science* **375**, 434–437 (2022).
- Z. Li et al., *Science* **376**, 416–420 (2022).
- M. V. Khenkin et al., *Nat. Energy* **5**, 35–49 (2020).
- S. M. Park et al., *Science* **381**, 209–215 (2023).
- G. Li et al., *Science* **379**, 399–403 (2023).
- G. Mani et al., *Langmuir* **24**, 6774–6784 (2008).
- P. Thissen, M. Valtiner, G. Grundmeier, *Langmuir* **26**, 156–164 (2010).
- E. Delamarche, B. Michel, H. Kang, C. Gerber, *Langmuir* **10**, 4103–4108 (1994).
- X. Wan et al., *J. Phys. Chem. C* **124**, 2531–2542 (2020).
- L. Li et al., *Nat. Energy* **7**, 708–717 (2022).
- W. Jiang et al., *Angew. Chem. Int. Ed.* **61**, e202213560 (2022).
- H. J. Yoon et al., *Angew. Chem. Int. Ed.* **51**, 4658–4661 (2012).
- J. Sun et al., *Sol. RRL* **5**, 2100663 (2021).
- E. Yalcin et al., *Energy Environ. Sci.* **12**, 230–237 (2019).
- R. Guo et al., *Adv. Funct. Mater.* **33**, 2211955 (2023).
- W. Wang et al., *Adv. Energy Mater.* **13**, 2300694 (2023).
- M. Li et al., *Nat. Commun.* **14**, 573 (2023).
- H. Zhang, C. Zhao, J. Yao, W. C. H. Choy, *Angew. Chem. Int. Ed.* **62**, e202219307 (2023).
- S. Y. Kim, S. J. Cho, S. E. Byeon, X. He, H. J. Yoon, *Adv. Energy Mater.* **10**, 2002606 (2020).
- I. Lange et al., *Adv. Funct. Mater.* **24**, 7014–7024 (2014).
- D. Di Girolamo et al., *Chem. Sci.* **11**, 7746–7759 (2020).
- F. Ma et al., *J. Energy Chem.* **52**, 393–411 (2021).
- Q. Lin, A. Armin, R. C. R. Nagiri, P. L. Burn, P. Meredith, *Nat. Photonics* **9**, 106–112 (2015).
- J. Wang et al., *Nat. Commun.* **11**, 177 (2020).
- M. Stollerfoht et al., *Adv. Mater.* **32**, e2000080 (2020).
- M. Stollerfoht et al., *Nat. Energy* **3**, 847–854 (2018).
- N. Phung et al., *ACS Appl. Mater. Interfaces* **14**, 2166–2176 (2022).
- F. Chen et al., *Nat. Energy* **8**, 839–849 (2023).
- X. Zhao et al., *Science* **377**, 307–310 (2022).

ACKNOWLEDGMENTS

Funding: This work was supported by the Innovation and Technology Fund (GHP/100/20SZ, GHP/102/20GD, MRP/040/21X), the ECS grant (21301319) and GRF grant (11306521) from the Research Grants Council of Hong Kong, Green Tech Fund (GTF202020164), the Science Technology and Innovation

obtained from biexponential fits, where k_B is Boltzmann's constant and T is aging temperature. The dashed line comes from the linear fits to extract the E_a from each exponential (left); and natural logarithm of AF versus $1/k_B T$. Standard operating condition for AF value calculation refers to 1-sun illumination at 25°C (right).

Committee of Shenzhen Municipality (SGDX20210823104002015, JCYJ20220818101018038). Zho.L. also acknowledges financial support from the National Natural Science Foundation of China (21975085) and Excellent Youth Foundation of Hubei Scientific Committee (2021CFA065). This work was authored in part by the National Renewable Energy Laboratory, operated by Alliance for Sustainable Energy, LLC, for the U.S. Department of Energy (DOE) under Contract DE-AC36-08G028308. The views expressed in the article do not necessarily represent the views of the DOE or the U.S. Government. **Author contributions:** Zhe.L., X.S., X.Z., and B.L. contributed equally to this work. Z.Z. conceived the ideas and designed the project with Zho.L., J.M.L., and X.Z. Z.Z. directed and supervised the research. Zhe.L. fabricated the devices, conducted the characterization, and analyzed the data. Zho.L. directed X.S. to design and synthesize the hole-selective molecule. B.L. and D.G. also contributed to the device fabrication, characterization, and data analyses. S.Z. conducted the DFT calculations. S.L. and J.G. also helped to fabricate the devices. Zhe.L., X.Z., B.L., Zho.L., J.M.L. and Z.Z. drafted, revised, and finalized the manuscript. All the authors revised the manuscript. **Competing interests:** Authors declare that they have no competing interests. The patent application been submitted. **Data and materials availability:** All data needed to evaluate the conclusions in the paper are present in the paper or the supplementary materials. **License information:** Copyright © 2023 the authors, some rights reserved; exclusive licensee American Association for the Advancement of Science. No claim to original US government works. <https://www.sciencemag.org/about/science-licenses-journal-article-reuse>

SUPPLEMENTARY MATERIALS

science.org/doi/10.1126/science.ade9637
Materials and Methods
Supplementary Text
Figs. S1 to S42
Tables S1 to S5
References (48–67)

Submitted 3 May 2023; accepted 6 September 2023
10.1126/science.ade9637